Applied Physics B (2019) 125:198
https://doi.org/10.1007/s00340-019-7309-6

**Applied Physics B**
**Lasers and Optics**

# Laser-cooled ytterbium-ion microwave frequency standard

S. Mulholland[1,2] · H. A. Klein[1] · G. P. Barwood[1] · S. Donnellan[1] · D. Gentle[1] · G. Huang[1] · G. Walsh[1] · P. E. G. Baird[2] · P. Gill[1,2]

Received: 15 November 2018 / Accepted: 17 September 2019 / Published online: 5 October 2019


**Abstract**
We report on the development of a trapped-ion, microwave frequency standard based on the 12.6 GHz hyperfine transition in laser-cooled ytterbium-171 ions. The entire system fits into a 6U 19-in. rack unit (51 × 49 × 28 cm) and comprises laser, electronics, and physics package subsystems. As a first step towards a full evaluation of the system capability, we have measured the frequency instability of our system which is $3.6 \times 10^{-12}/\sqrt{\tau}$ for averaging times between 30 and 1500 s.

## 1 Introduction

The current state of the art of portable microwave clocks and frequency standards are based on beam tubes [1], vapor cells [2, 3], and trapped ions in buffer gas [4–6]. In beam-tube clocks, the linewidth of the atomic resonance is proportional to the length of the beam tube and this places limits to the extent to which they can be miniaturized. In addition, the atom flux in a beam tube is thermal which limits performance by the second-order Doppler effect, and the magnets that provide state selection produce magnetic inhomogeneities along the beam path that result in a difficult to characterize second-order Zeeman shift. Vapor-cell clocks are sensitive to the cell temperature and pressure, their output frequency drifts on timescales longer than approximately 1 day, and long-term aging phenomena affect the frequency [7]. Buffer-gas cooled trapped-ion systems are susceptible to collisional and pressure related shifts that limit long-term stability and accuracy [8–10]. The use of thermal atoms in these systems also limits frequency reproducibility. To reduce these effects, the highest-performance laboratory clocks, such as cesium fountains [11–13], use laser cooling in an ultra-high vacuum (UHV).

We report on the development of a laboratory prototype system for a compact, trapped-ion, microwave frequency standard incorporating laser cooling. The system is shown in Fig. 1 and is housed in a 6U 19-in. rack (51 × 49 × 28 cm).

Non-portable laboratory versions of laser-cooled, ytterbium-ion, microwave frequency standards have been built [14, 15], and it is estimated that a potential fractional-frequency instability of $5 \times 10^{-14}/\sqrt{\tau}$ and fractional-frequency uncertainty of $\sim 5 \times 10^{-15}$ are achievable in laboratory systems [10, 14]. Clock applications at this level of performance include network synchronization, navigation, and accurate timing capabilities independent of Global Navigation Satellite Systems (GNSS).

In this paper, our trapped-ion microwave frequency standard is described. The apparatus (physics package, lasers, and electronics) is outlined in Sect. 2, and the methods of operating the frequency standard are described in Sect. 3. The results achieved to date, and an analysis of the limitations to stability and accuracy of our frequency standard, are presented in Sect. 4.

## 2 System overview

The frequency standard [16] consists of three main subsystems: ions are created, trapped, and probed within an evacuated linear ion trap system; all the required lasers and optics with the exception of a wavemeter are housed in a 6U pullout rack unit. The 6U rack also contains the electronics and microwave system that runs the operational sequence and locks an oscillator to the atomic resonance. These systems are detailed in the following subsections. During normal clock operation, when the oven is not being fired, the system consumes a maximum power of only 80 W.

✉ S. Mulholland
sean.mulholland@npl.co.uk

[1] National Physical Laboratory, Teddington TW11 0LW, UK

[2] Clarendon Laboratory, University of Oxford, Oxford OX1 3PU, UK

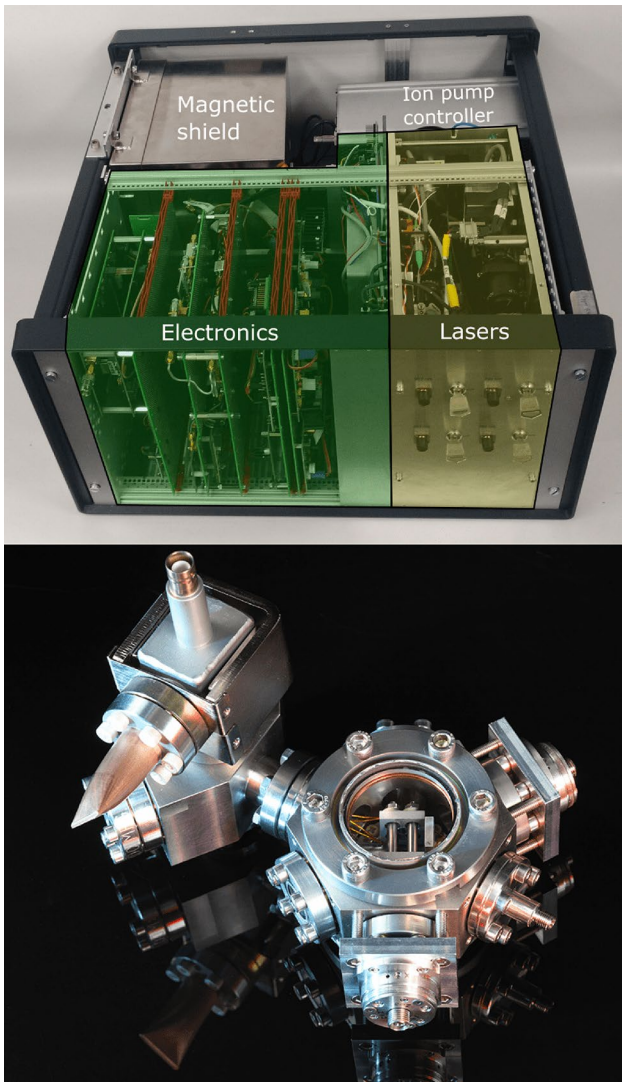


**Fig. 1** Labeled photograph of the frequency standard within the 6U, 19-in. rack case (top) and the vacuum chamber (bottom). The majority of the electronics is located on the vertical 6U cards at the front left of the case. The laser system is housed at the front right of the case. The physics package, within a magnetic shield, is located at the back left. The ion pump controller is visible at the back right. A power supply (not shown) is at the rear. The vacuum chamber houses the ion trap, pumps, and electrical feedthroughs. Not shown on the image are the PMT, imaging optics, and coils that are rigidly mounted to the chamber. In addition, we fitted a soft iron enclosure around the ion pump to confine the magnetic field from the pole pieces

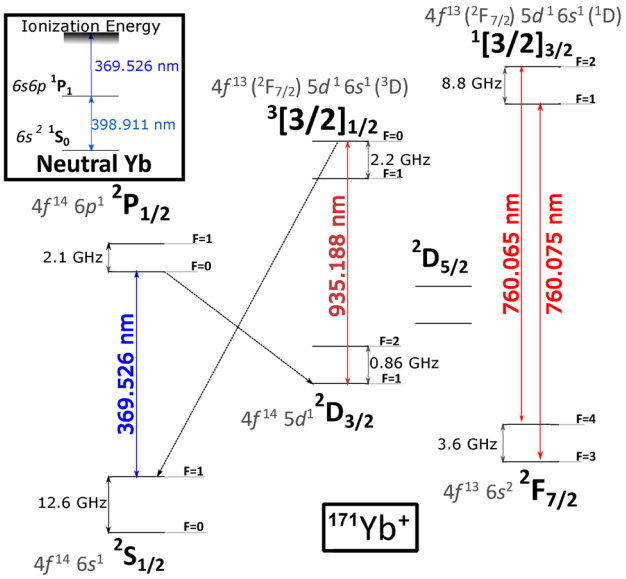


**Fig. 2** Partial term schemes showing the driven atomic transitions and the required laser wavelengths and microwave frequencies. The inset shows the transitions in neutral ytterbium used for photoionization. The main diagram shows the $^{171}Yb^+$ term scheme

The term schemes showing the atomic transitions used in the frequency standard for both neutral and singly-ionized $^{171}$Yb are shown in Fig. 2.

To laser cool the ions, microwaves at 12.6 GHz are applied and a 369 nm laser is tuned to the $F = 1 \rightarrow F' = 0$ component of the $6s\ :\ ^2S_{1/2} \rightarrow 6p\ :\ ^2P_{1/2}$ transition. To mix the ground states during cooling, the microwave transition is driven rapidly with a Rabi frequency of 100 kHz. The cooling transition is a strong, dipole-allowed transition with a natural linewidth, $\gamma_{369}$, of 19.6 MHz full width at half maximum (FWHM) [17]. The cooling cycle is not completely 'closed', since the upper state can decay with a probability of about $^1/_{200}$ into a $^2D_{3/2}$ state with a 50 ms lifetime [18]. To prevent 'shelving' the ions in this state, a laser of 935 nm is tuned to the $^2D_{3/2}(F = 1) \rightarrow {}^3[^3/_2]_{1/2}(F' = 0)$ transition. During laser cooling, the detected ion fluorescence rate of the 369-nm transition is $1.5 \times 10^5$ counts/s from 300 ions, which corresponds to each of the ions scattering approximately $2 \times 10^4$ photons/s taking into account our collection efficiency of 2.7%.

Ytterbium has a low-lying F state with a natural lifetime of the order of 10 years [19]. The long lifetime can be exploited to provide a narrow linewidth for an optical clock [20, 21]. However, population trapping in the F state can occur by a collisional mechanism, and this can degrade the performance of a clock [8, 22]. To avoid this, we took the precaution of including a 760 nm laser in our system. In addition, the frequency standard operates under UHV (typically $< 10^{-10}$ mbar is measured by the ion pump controller) and the collisional route into the F state is suppressed. We did not observe significant population trapping in the F state, even when operating without the 760 nm laser.

The laser cooling of $^{171}Yb^+$ has a further complication. In the absence of an external magnetic field, the ions will become optically pumped in the $^2S_{1/2}, F = 1$ dark states. A magnetic field of 700 μT was applied by a coil to induce a precession of the ions' dipole moments to destabilize the

dark states [23]. This large magnetic field must be turned off during the probe phase of the clock cycle to reduce the uncertainty in the second-order Zeeman shift. When switched off, the magnetic field falls to 1% of its full value within 12 ms, limited by eddy currents.

The Doppler limit for laser cooling is around 0.5 mK [17, 24]. However, confining large clouds of ions in a quadrupole linear RF trap inevitably leads to significant micromotion, and therefore, the ion temperatures were higher than this Doppler limit.

## 2.1 Physics package

The physics package comprises a linear ion trap within a vacuum housing and is mounted inside a mu-metal magnetic shield. A photomultiplier (PMT) with imaging optics, magnetic bias coils, and fiber optic collimators are attached outside the vacuum chamber.

The ion trap comprises four rods and five plate electrodes, as shown in Fig. 3. The rods provide trapping in the radial direction, and a pair of plates confine the ions axially. Two orthogonal plate electrodes are used to compensate for stray DC fields and minimize radial micromotion. The final-plate electrode is grounded. The plates are isolated from each other by polyether ether ketone (PEEK) washers. The trap assembly was screwed into internal mounting holes in the vacuum chamber with PEEK screws. The oven, which provides the source of neutral ytterbium atoms, is embedded within a ceramic housing in an electrode. The front of the oven was spot-welded on the horizontal compensation electrode. The dimensions of the ion trap are summarized in Table 1. The ratio of the rod electrode radius to the ion-electrode separation, $r_e/r_0$ was 0.63, which is less than the value of approximately 1.145 that gives the best approximation to a quadrupolar electric field [25, 26]. Departing from the ideal quadrupolar field causes an increase in orbits within the ion trap that are unstable, and gain energy from the trapping field [27].

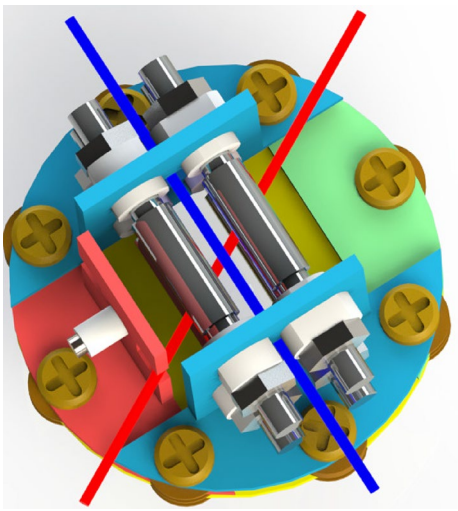

**Fig. 3** Three-dimensional illustration of the ion trap with the laser paths shown. The electrodes are colored for identification: endplates: blue, horizontal compensation: red, vertical compensation: yellow, ground: green. The oven is embedded, within an alumina insulator, in the horizontal compensation electrode. The four rods are isolated from the endplates by alumina bushes. The axial laser beam contains the UV wavelengths and passes through holes bored in the endplates. The IR laser beam is 60° to the axis and passes through a cut-out on the electrode that houses the oven. PEEK washers are used to isolate the plates and PEEK screws attach the ion trap to the vacuum chamber

As this device was designed to be transportable, it was essential that the various optical elements be robustly mounted. The laser launchers, PMT, and magnetic shields are all directly mounted onto the vacuum chamber. The vacuum chamber was made from titanium as it is non-magnetic and exhibits low outgassing. The fused silica windows were a low-profile design and indium-sealed to titanium flanges. The vacuum system was baked at 130 °C for a week while connected to a turbo-molecular pump to remove outgassing material sorbed to the chamber walls. Indium seals on the windows limited the baking temperature. After bake out, the internal getter pump was activated, and the external pump was valved off and removed. Getter pumps do not pump noble gases, so, for long-term operation, an ion pump was also used.

## 2.2 Laser system

The laser system [28] comprises four lasers: 369 nm, 760 nm, 798 nm, and 935 nm. Of these lasers, the 935 nm and 760 nm are commercially available as distributed feedback (DFB) devices as they are used in gas-sensing applications. The 798 nm is a volume holographic grating (VHG) extended cavity diode laser (ECDL) [29] and is frequency doubled to 399 nm in a periodically poled nonlinear waveguide. The 369 nm was provided by an ECDL.

The laser beams are transmitted from the laser system by polarization-maintaining (PM) fibers to fiber launchers that are fixed to the vacuum chamber. These send the UV beam down the trap axis and the IR at 60° to the axis. Both beams

**Table 1** Ion trap parameters

| | |
|---|---|
| Rod electrodes | Titanium electrodes, radius, $r_e = 2$ mm |
| Endcap electrodes | Aluminum plates separated by 17.8 mm |
| Rod spacing | 7.3 mm center-to-center |
| Laser access | On-axis 4.8 mm diameter bore through endplates. 3.5 × 4 mm notch in oven holder 60° to axis |
| Ion-electrode separation, $r_0$ | 3.16 mm |
| $r_e/r_0$ | 0.63 |

are focused to a waist at a position after the ions. At the ions, the 1 / *e* intensity radius is 200 µm for the 369-nm laser and 300 µm for the 935-nm laser.

Although it is advantageous for the beams to travel down the trap axis as it ensures the best overlap with the ions, it was simpler to send the IR and UV beams through separate windows.

## 2.3 Electronics and microwave package

The electronics system comprises the power supplies, microwave frequency generation, and experiment control. NPL-designed low-noise current sources are used for both the 369 nm laser and the Helmholtz coils. These current sources are a modification of a Hall–Libbrecht design [30, 31]. The current sources that are used for the other lasers are commercial devices. The lasers are temperature controlled by an NPL-designed temperature controller. The RF trap drive is based on a circuit developed by Sandia [32].

A field-programmable-gate-array (FPGA) controls the experimental sequence. A graphical user interface (GUI) allows the experimental sequences and timings to be altered from a laptop computer.

The frequency chain to produce the 12.6 GHz clock frequency from a 10 MHz quartz (Rakon HSO 13) local oscillator is shown in Fig. 4. This frequency chain multiplies a 10 MHz input up to 12.8 GHz. This 12.8 GHz signal is split into two paths: the first path is divided by 16 to clock two direct digital synthesizers (DDSs) (Analog Devices AD9912) and the second path is sent into a mixer. The second input of the mixer is a signal of around 158 MHz that is used to generate the clock frequency as the low-frequency sideband of the mixer output. The 12.8 GHz and the high-frequency sideband are then removed by a band-pass filter, and the clock frequency is then applied to the ions via an antenna.

The power of the applied microwaves can be controlled in the switching network of two single-pole-double-throw (SPDT) switches which provide up to 130 dB of dynamic range between the high-power state, used for laser cooling, and the low-power state, used for state preparation and probing the clock transition.

An error signal is derived, through modulating the probe frequency to measure the high- and low-frequency sides of

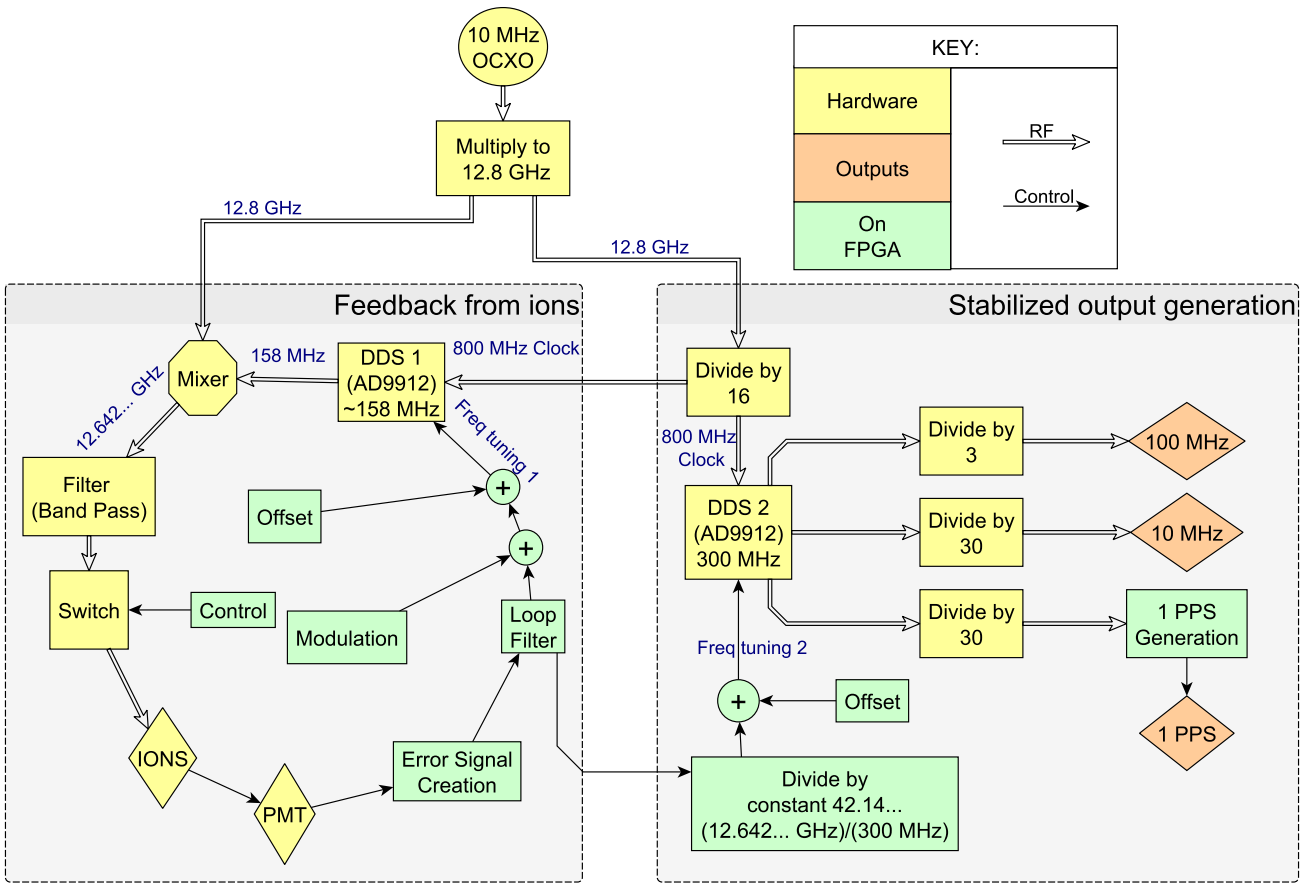


**Fig. 4** Schematic of the frequency chain. The frequency chain produces both the 12.6 GHz for driving the clock transition and the stabilized clock outputs from a free-running 10 MHz LO

the resonance, and the frequency offset between the free-running frequency chain and the ions is determined. This frequency offset is used for both locking 12.6 GHz to the ions and for providing the stabilized RF outputs.

The stabilized RF outputs are generated by updating DDS2 (Fig. 4) that outputs 300 MHz. The frequency corrections that are calculated by the feedback loop at 12.6 GHz are divided by a constant (12.6418 … GHz/300 MHz ≈ 42.14) to ensure the appropriate fractional change. This removes the drift from the free-running frequency chain and transfers the stability from the ions' frequency discriminant to the clock output. The AD9912 DDSs have a resolution of 4 µHz, which means that the RF outputs can be tuned with a fractional-frequency resolution of $1.4 \times 10^{-14}$, the fractional-frequency resolution of the probe frequency at 12.6 GHz is $4 \times 10^{-16}$.

This all-digital method relaxes the requirements for the tuning characteristics of the LO, and means that designing a low-noise analog voltage-tuning circuit is not required.

## 3 Method of operation

At the beginning of a measurement, the lasers are frequency-stabilized by locking to a wavemeter that is external to the 6U 19-in. rack [33] and a few hundred ions are loaded by passing a current through an oven in the presence of 399 nm and 369 nm light. The LO is then locked to a Rabi resonance from the trapped ions. The measurement cycle consists of four stages: laser cooling, state preparation, clock pulse, and state-detection.

During the state-detection stage, a neutral density filter is moved into the 369-nm beam to reduce the intensity to below the saturation level. This has the dual benefits of both reducing the number of photons scattered off the compact trap and vacuum apparatus and also increasing the number of signal photons by suppressing the off-resonantly driven $^2S_{1/2}(F=1) \rightarrow 6p : {}^2P_{1/2}(F'=1)$ non-cycling transition. The contrast of the detected feature is also limited by incomplete state preparation that results from the $^2S_{1/2}(F=0) \rightarrow 6p : {}^2P_{1/2}(F'=1)$ transition being driven at 10% of the rate of the resonant $^2S_{1/2}(F=1) \rightarrow 6p : {}^2P_{1/2}(F'=0)$ transition. It is thought that this large off-resonant transition rate is due to amplified spontaneous emission from the 369-nm ECDL; this effect has been reported for similar 393-nm UV laser that is used in calcium ion systems [34]. The cycle time is dominated by the clock pulse and laser cooling, which for the data presented were both 4 s in duration. Figure 5 shows the states of the apparatus during each of these stages of the measurement.

A linear drift-insensitive digital integrator feedback scheme is used to find the new frequency of the offset of the LO, $f_i$, from the previous frequency, $f_{i-1}$, and the fluorescence imbalance between the low and high-frequency probe frequencies ($S_L - S_H$). The two probe frequencies are offset from $f_{i-1}$ by the same amount in the low- and high-frequency sides of the resonance. The gain, $g$, is calculated from a fit to the Rabi resonance. The feedback loop is made insensitive to a linear signal-level drift by probing the high- and low-frequency sides of the resonance twice before applying a correction, in a pattern: low, high, high, and then low:

$$f_i = f_{i-1} + \frac{g}{2}(S_{L1} + S_{L4} - S_{H2} - S_{H3}). \quad (1)$$

The gain is divided by two in Eq. (1), because both sides of the line are sampled twice before a correction is made.

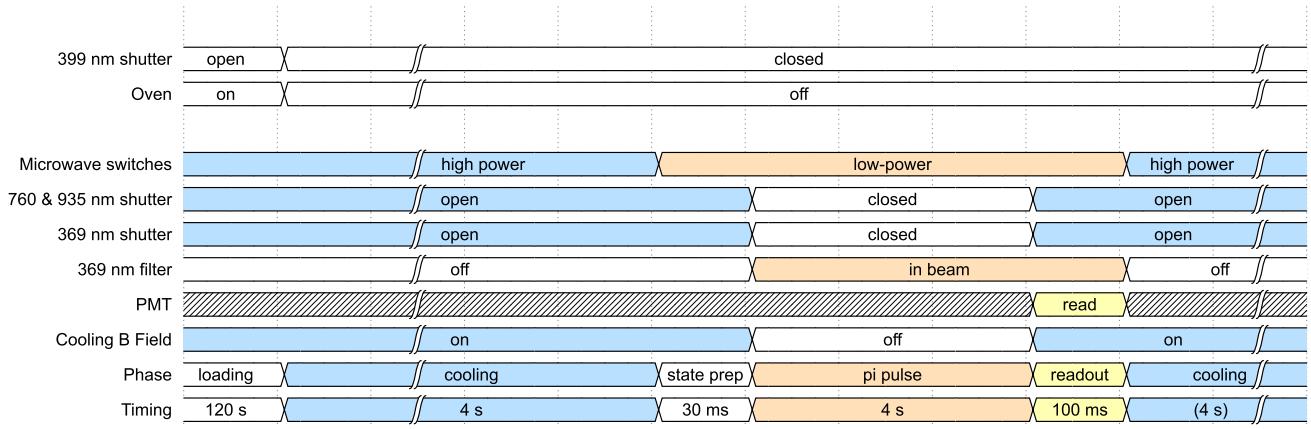


**Fig. 5** Clock measurement sequence, showing the states of the hardware elements during the measurement cycle, and the timings used for the measurements presented. The low-power microwaves are attenuated by 130 dB from the high-power state. The cycle time of ≈ 8 s is dominated by the cooling and clock pulse times

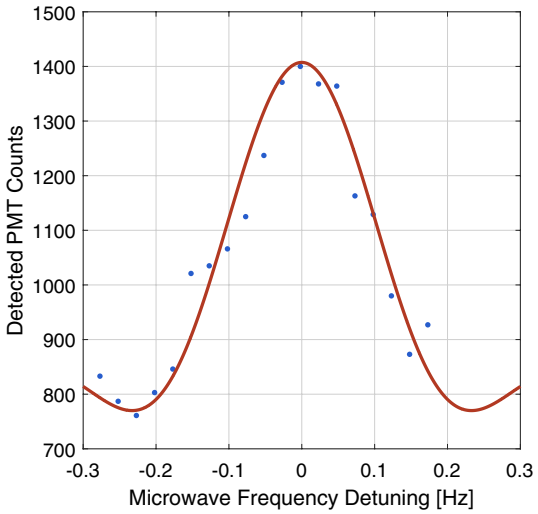


**Fig. 6** Measured Rabi lineshape. The data were obtained from a single scan with a microwave pulse length of 4 s and detection time 100 ms. The frequency scale is relative to the peak of the resonance, offset from the unperturbed frequency by about 2 Hz. These data were taken at the beginning of the stability measurement

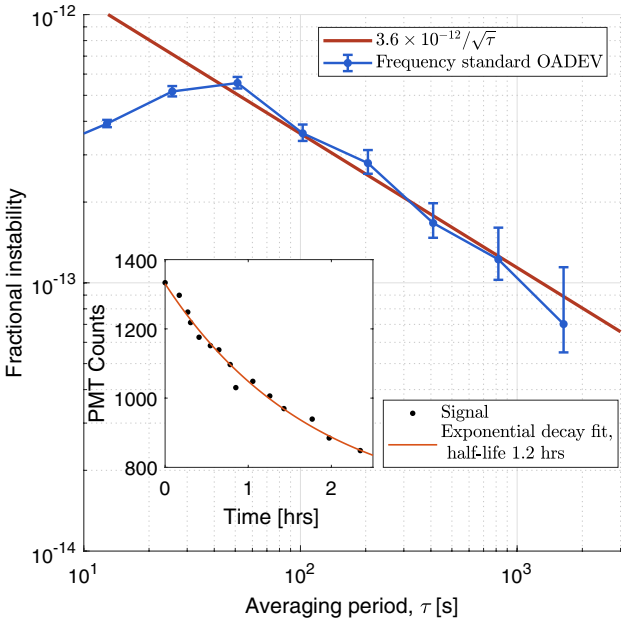


**Fig. 7** Stability of the frequency standard measured against a hydrogen maser. The fractional overlapping Allan deviation (OADEV) is plotted against averaging time. An instability of $3.6 \pm 0.2 \times 10^{-12}/\sqrt{\tau}$ is measured between averaging times of 30–1500 s. Signal loss, shown in the inset, limits the data to $2^1/_4$ h

## 4 Results

A Rabi lineshape was measured by sweeping the microwave frequency through the resonance, and this is shown in Fig. 6. Following the frequency sweep, the microwaves were then locked to the resonance. The lock to the clock transition produces a stabilized 10 MHz output signal and this was compared with the 10 MHz signal from a maser via a phase comparator (Microsemi 3120A). The phase difference was logged as a function of time, and the Allan deviation was calculated and displayed in real time on a PC.

Figure 7 shows frequency stability data taken over a continuous period of $2^1/_4$ h. During the measurement, the signal level was decreasing with a half-life of 1.2 h. This resulted in increased instability from shot noise as discussed in the following section. An instability of $3.6 \pm 0.2 \times 10^{-12}/\sqrt{\tau}$ for averaging times between 30 and 1500 s was measured.

The following sections detail the causes of instability that affect the performance of this frequency standard. These include shot noise when measuring the clock transition, which limits the stability for the data presented, and instabilities due to changing environmental parameters that must be controlled for long-term stability performance. The results of this analysis are summarized in Table 2.

### 4.1 Shot noise and dead time

From the scan over the Rabi feature that was taken at the beginning of the measurement, the shot-noise limit to the instability was estimated as $\sigma_{\mathrm{SN}}(\tau) \approx 1 \times 10^{-12}/\sqrt{\tau}$ using the formula [35]:

$$\sigma_{\mathrm{SN}}(\tau) \approx \frac{\sqrt{\tau_{\mathrm{p}} + \tau_{\mathrm{d}}}}{\pi \cdot \mathrm{SNR} \cdot Q} \times \frac{1}{\sqrt{\tau}}. \tag{2}$$

The clock transition was probed for $\tau_{\mathrm{p}} = 4$ s and there was $\tau_{\mathrm{d}} = 4$ s of cooling time between measurements. The signal-to-noise ratio at the peak (SNR) was estimated as 16 using the formula:

$$\mathrm{SNR} \approx \frac{\mathrm{SH}}{\sqrt{\mathrm{BG} + \mathrm{SH}}}, \tag{3}$$

where SH is the signal level above the background at the maximum point and BG is the background signal level that arises from light scattered from the ion-trap electrodes, and incomplete state preparation.

The quality factor ($Q$) was $6.32 \times 10^{10}$ from the FWHM of 0.2 Hz and the transition frequency of 12.6 GHz. Signal loss caused the SNR to decrease exponentially over time with a half-life of 1.2 h and so the instability was higher than that estimated from the initial Rabi resonance. It is believed that this signal loss is due to molecular ions forming by the ytterbium ions chemically reacting with gases that are released into the vacuum system when the ytterbium source is heated.

The pressure in the vacuum system was measured by monitoring the current drawn from the ion pump controller.

These currents are a few nanoamperes and there is a large uncertainty in the derived pressure. During clock operation, the reported pressure was below $10^{-10}$ mbar, but when the oven is heated to load ions into the trap, this rises to $1 \times 10^{-9}$ mbar.

At $< 10^{-10}$ mbar, the expected ion-neutral collision rate is 15 per ion per hour using the Langevin model for ion-neutral atom collisions [36, 37]. Ytterbium single-ion optical clocks have shown ion lifetimes greater than 1 month [38], but ytterbium ions are known to react rapidly with $H_2O$ and $O_2$ molecules [39], and these gases may be emitted when the oven is heated. A new oven design with a lower operating current and improved thermal isolation is undergoing tests and this shows much lower levels of fluorescence loss.

### 4.2 Second-order Zeeman shift

As the clock transition has no linear Zeeman shift at zero magnetic field, the frequency sensitivity to magnetic fields is primarily from the second-order Zeeman effect. For $^{171}Yb^+$, this is [40]:

$$\frac{\Delta\nu_{2OZ}}{B^2} = 31.08[\mathrm{mHz}/(\mu\mathrm{T})^2] \tag{4}$$

Small DC fluctuations, $\mathbf{\delta B}$, on a background magnetic field, $\mathbf{B}$, result in changes to the second-order Zeeman shift, $\delta\nu_{2OZ}$, given by:

$$\frac{\delta\nu_{2OZ}}{\nu_{\mathrm{clock}}} = 4.92 \times 10^{-12}\,[\mu\mathrm{T}^{-2}]\,\mathbf{B}\cdot\mathbf{\delta B}, \tag{5}$$

to first order in $\mathbf{\delta B}$.

A stable magnetic field giving rise to a constant second-order Zeeman shift is not a problem, provided that it is corrected for; fluctuating magnetic fields provide a greater challenge. To mitigate this effect, the scalar product of the terms $\mathbf{B}$ and $\mathbf{\delta B}$ is minimized by making these vectors orthogonal. $\mathbf{B}$ is reduced by adjusting the currents in three orthogonal sets of Helmholtz coils to null the background magnetic field. Subsequently, a small and well-controlled bias of 8 μT is applied to define the quantization axis. At this bias field, the second-order Zeeman shift is about 2 Hz, and to first order, the fractional-frequency sensitivity to magnetic field fluctuations parallel to the bias field is $4.0 \pm 0.1 \times 10^{-11}/\mu\mathrm{T}$. The $\mathbf{\delta B}$ term is minimized by operating the trap in a magnetic shield with a DC shielding factor parallel to the bias field of $40 \pm 4$ (and approximately 750 and 20 in the two perpendicular directions), and using low-noise power supplies to drive the Helmholtz coils.

Both the background magnetic field in the laboratory, and the current passing through the quantization-axis coils, were measured to determine the instability of the second-order Zeeman shift. The magnetic field in the laboratory was measured with a fluxgate magnetometer, outside the magnetic shields, a few centimeters away from the ion trap. The coil current was measured across a 20 Ω precision resistor on a voltmeter.

The instability in the second-order Zeeman shift is shown on Fig. 8 and the results are summarized in Table 2. The instability due to fluctuating magnetic fields is small compared to the instability from the shot noise. There is also an AC second-order Zeeman shift that arises from oscillating magnetic fields [41]. The oscillating magnetic fields are primarily from two sources, 50 Hz mains AC and the RF trap drive. The 50 Hz field was measured using the fluxgate magnetometer. This sensor is sensitive to oscillations below a few hundred Hertz and an oscillating magnetic field with amplitude 10 μT at 50 Hz was measured parallel to the quantization axis. Assuming that the 50 Hz shielding factor is similar to the DC value, this results in a frequency shift of $8 \pm 1 \times 10^{-14}$ and an instability that is negligible over the timescales of our frequency stability measurement.

The trap capacitance causes small oscillating currents at the trapping frequency in the trap rods. For a perfectly symmetric trap, the magnetic fields generated by these currents will cancel along the nodal line of the trapping field. However, if the ions are not centered, or if the currents are not symmetric, an oscillating magnetic field will cause an AC Zeeman shift [41, 42]. The fractional-frequency shift from this effect was calculated to be below $1 \times 10^{-15}$.

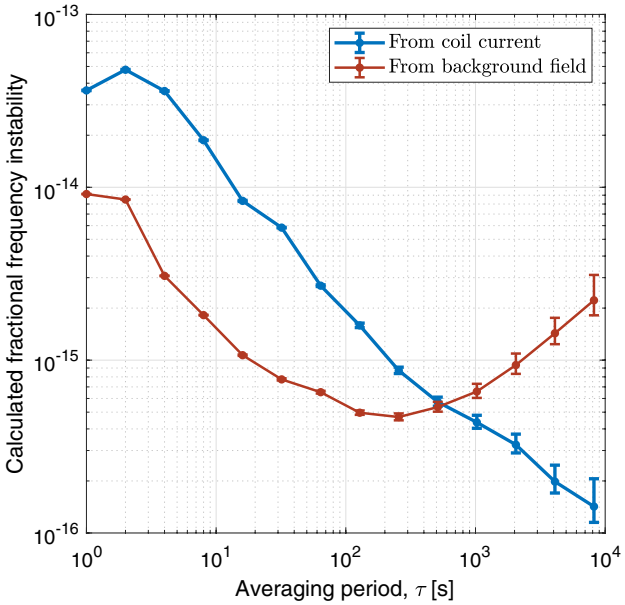


**Fig. 8** Calculated second-order Zeeman instability from the measured fluctuations in both the background magnetic field of the laboratory (red trace) and the magnetic field from the bias coils (blue trace). The drift in the background field that is evident after a few hundred seconds could be removed or corrected for by a control system

### 4.3 Second-order Doppler shift

The frequency shift due to the second-order Doppler effect is given by:

$$\Delta\nu_{2OD} = -\frac{\nu}{2} \times \frac{u^2}{c^2}, \tag{6}$$

where $\nu$ is the center frequency of the resonance, $u$ is the velocity of the ion, and $c$ is the speed of light.

A measurement of the ion velocities was made by observing the first-order Doppler shift on the 369 nm cooling transition. The laser detuning was scanned from the red side of the resonance towards line center both when the ions were continuously cooled and when the laser was extinguished for 4 s between measurements to simulate a clock measurement. The results are shown in Fig. 9. As may be expected from a cloud of ions, it is evident that there is significant micromotion [43, 44]. To calculate the second-order Doppler shift, the root-mean-square (rms) velocity was calculated by numerical integration of the velocity distributions implied from these scans over the cooling transition. These calculated velocities are over-estimates as the method assumes that all the broadening of the transition is due to first-order Doppler shifts and because laser heating effects have suppressed the fluorescence of the ions at small detunings. Between measurements, the laser is not returned to line center and the effect of this incomplete recooling will also contribute to an over-estimate of the rms velocity. From these measurements, the second-order Doppler shift was estimated to be below $-2.0 \pm 0.5 \times 10^{-14}$ and have an instability less than $5 \times 10^{-15}$.

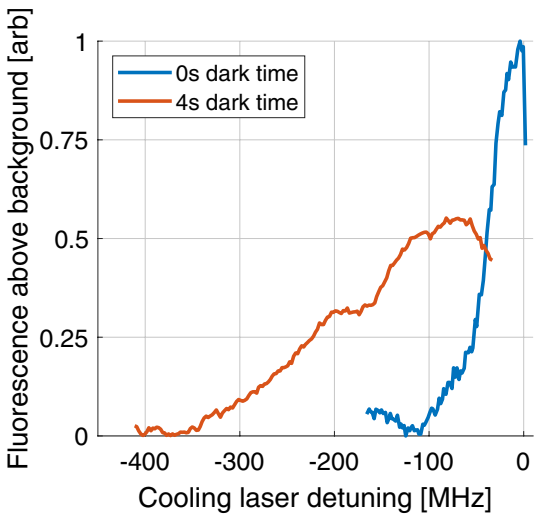


**Fig. 9** Doppler broadened profiles of the laser-cooling transition. The trace in blue shows the fluorescence profile with no dark time and can be used to infer a rms velocity of $18 \pm 2$ m/s. Each of the points on the orange trace is a measurement immediately after a 4 s period where the cooling laser was blocked. To avoid cooling the ions, the measurements were taken within 10 ms of the cooling laser becoming unblocked. From the profile of the transition, the rms velocity after the clock pulse is calculated to be $55 \pm 10$ m/s. These rms velocities are likely to be over-estimates for reasons that are explained in the text. The y-axis scale is relative to the peak fluorescence with no dark time, the background from light that is not scattered by the ions is removed

### 4.4 Quadratic Stark shift

The quadratic Stark shift from the RF trapping field is given by [45]:

$$\frac{\Delta\nu_{\text{AC Stark}}}{\nu_{\text{clock}}} = -k_s \langle \boldsymbol{E}^2 \rangle \tag{7}$$

$$= -4k_s \left(\frac{\omega_{\text{single}}}{\omega_{\text{cloud}}}\right)^2 \frac{m\Omega_{\text{trap}}^2}{e^2} k_B T, \tag{8}$$

where $e$ is the elementary charge and $\Omega_{\text{trap}}$ is the RF trap frequency. The value of the coefficient $k_s$ has been measured experimentally [46] to be $k_s = 2 \pm 1 \times 10^{-21}\ \text{m}^2\text{V}^{-2}$. The trap drive frequency was $(2\pi) \times 2$ MHz, and the peak-to-peak voltage was 300 V. The ratio of the single-ion and cloud secular frequencies $\frac{\omega_{\text{single}}}{\omega_{\text{cloud}}}$ was measured to be $1.0 \pm 0.1$. The resulting fractional-frequency offset is $2 \pm 1 \times 10^{-15}$ and instability from the quadratic Stark shift is at the $10^{-15}$ level.

### 4.5 Black-body radiation (BBR) shift (AC Stark shift)

There is an AC Stark shift due to the thermal radiation produced by the ions' surroundings, $T$, given by [47]:

$$\frac{\Delta\nu_{\text{BB}}}{\nu_{\text{cloud}}} = \beta \left(\frac{T}{T_0}\right)^4 \left[1 + \epsilon \left(\frac{T}{T_0}\right)\right]^2, \tag{9}$$

where $T_0$ is the room temperature and 300 K and the coefficients are [47, 48] $\beta = -9.83 \times 10^{-16}$, and $\epsilon = 2 \times 10^{-3}$.

An estimate of the fractional-frequency shift from BBR of $-1.0 \pm 0.1 \times 10^{-15}$ is obtained by assuming a 20 K range in temperature for the ions' surroundings, from 300 to 320 K. A fractional-frequency sensitivity to the temperature close to 310 K is calculated to be $-1 \times 10^{-17}/\text{K}_{\text{T}\approx 310K}$. Assuming that an unstable temperature at the 10 K level gives an estimate of the fractional-frequency instability of the BBR shift of $< 1 \times 10^{-16}$.

### 4.6 Dick effect

In the measurements reported in this paper, the duty cycle—defined as the fraction of the measurement devoted to probing the transition—was 1/2. Due to the ions not being

**Table 2** Summary of the sources of noise, frequency uncertainty, and frequency offsets during this frequency stability measurement. Further details are within the referenced sections of the text

| Effect | Parameter values | Fractional frequency | | |
|---|---|---|---|---|
| | | Sensitivity | Offset | Instability |
| Shot noise and dead time | 650 initial signal and 750 background photons, duty cycle 1/2, signal loss with half-life 1.2 h [Sect. 4.1] | – | – | $3.6 \pm 0.2 \times 10^{-12}/\sqrt{\tau}$<br>$30 < \tau < 1500$ s |
| Second-order Zeeman: coils | $B_{\text{bias}} = 8.0 \pm 0.2\,\mu\text{T}$ [Sect. 4.2] | $4.0 \pm 0.1 \times 10^{-11}/\mu\text{T}$ | $1.60 \pm 0.08 \times 10^{-10}$[a] | $< 1 \times 10^{-13}$<br>$1 < \tau < 10^2$<br>$1.4 \pm 0.1 \times 10^{-14}/\sqrt{\tau}$ s<br>$10^2 < \tau < 10^4$ s [Fig. 8] |
| Second-order Zeeman: background DC | $B_{\text{lab}} \approx 50\,\mu\text{T}$<br>Shielding factor $= 40 \pm 4$ [Sect. 4.2] | $1.0 \pm 0.1 \times 10^{-12}/\mu\text{T}$ | Nulled by coils | $< 1 \times 10^{-14}$<br>$1 < \tau < 10^4$ s [Fig. 8] |
| AC Zeeman | $B_{50\,\text{Hz}} < 0.25\,\mu\text{T}$<br>$B_{\Omega} < 20\,\text{nT}$ [Sect. 4.2] | $2.5 \times 10^{-12}/(\mu\text{T})^2$ | $8 \pm 1 \times 10^{-14}$ (50 Hz)<br>$< 1 \times 10^{-15}$ ($\Omega$) | $< 1 \times 10^{-15}$ |
| Second-order Doppler | $v_{\text{rms}} \approx 18$ m/s $\rightarrow$ 55 m/s [Sect. 4.3] | $-5.6 \times 10^{-18}/v_{\text{rms}}^2$ | $-2.0 \pm 0.5 \times 10^{-14}$ | $< 5 \times 10^{-15}$ |
| Quadratic Stark shift: trap drive | $\Omega = 2$ MHz, $V_{\text{pk-pk}} = 300$ V [Sect. 4.4] | $< 1 \times 10^{-16}/V_{\text{pp}}$ | $2 \pm 1 \times 10^{-15}$ | $< 1 \times 10^{-15}$ |
| BBR shift | $300 \le T_{\text{trap}} \le 320$K [Sect. 4.5] | $-1 \times 10^{-17}/\text{K}_{\text{T}\approx 310\text{K}}$ | $-1.0 \pm 0.1 \times 10^{-15}$ | $< 1 \times 10^{-16}$ |
| Dick effect | Duty cycle 1/2, feedback at 30 s [Sect. 4.6] | – | – | $\sim 1 \times 10^{-13}/\sqrt{\tau}$ |

[a]This uncertainty is due to the method used to measure the second-order Zeeman shift during this stability measurement. For a full-accuracy implementation of our clock, we would monitor this shift using the $F = 1$, $m_F = \pm 1$ magnetically sensitive Zeeman components of the clock transition and this uncertainty could be reduced to below $1 \times 10^{-14}$

continuously measured, some high-frequency noise on the oscillator will be aliased to lower frequencies and will add instability to each clock measurement. The instability added for a duty cycle of 1/2 was calculated by Dick [49] as 1.4 times below the local oscillator instability at the measurement time. As the instability from shot noise from the ion signal was greater than the instability from the LO at the measurement time, we are not limited by the Dick effect.

## 5 Future developments

The most significant limitation to the performance of the prototype described in this paper arises from signal loss via an accumulation of non-fluorescing (dark) ions that appear to be molecular ions formed by $^{171}\text{Yb}^+$ reacting with background gas. Attempts to recover fluorescence using either 760 nm light at F state repump frequencies that we measured from a $\text{Yb}^+$ [28] [760.065(1) nm and 760.075(1) nm], or the $\text{YbH}^+$ dissociation wavelength—369.482 nm [50], were not successful. The observation that the dark ions accumulate primarily on the radial edges of a Coulomb crystal as seen in Fig. 10 implies that the dark ions are heavier than $^{171}\text{Yb}^+$, and so, we conclude that they are most likely to be Yb molecular ions. This separation occurs, because the central ion-trapping force is stronger for lighter ions than heavier ions [51, 52]. Identification via molecular mass determination from the secular frequencies [39, 53] is not straightforward on account of the large $^{171}\text{Yb}^+$ mass.

Investigations are ongoing as ion loss clearly impacts on both long-term frequency stability, and operational time, and reduces the efficiency of the laser cooling. Before the dark ions form, it takes 500 ms for the fluorescence to recover after the cooling laser is blocked for 4 s during a clock pulse. This recovery time increases as the number of dark ions increases. To ensure consistent cooling, we use a conservative cooling time of 4 s.

The mounting and heatsinking of our oven are also undergoing design changes and preliminary off-line tests indicate significant performance improvements. Our new oven arrangement requires considerably less current, and we believe that this will lead to reduced ion loss and more rapid ion re-loading in a future trap system. Reduced oven currents can also be expected to lead to reduced changes in ambient magnetic field on loading and so improve load-to-load frequency reproducibility. This short-term reproducibility (system re-trace) is currently limited at the $2 \times 10^{-13}$ level

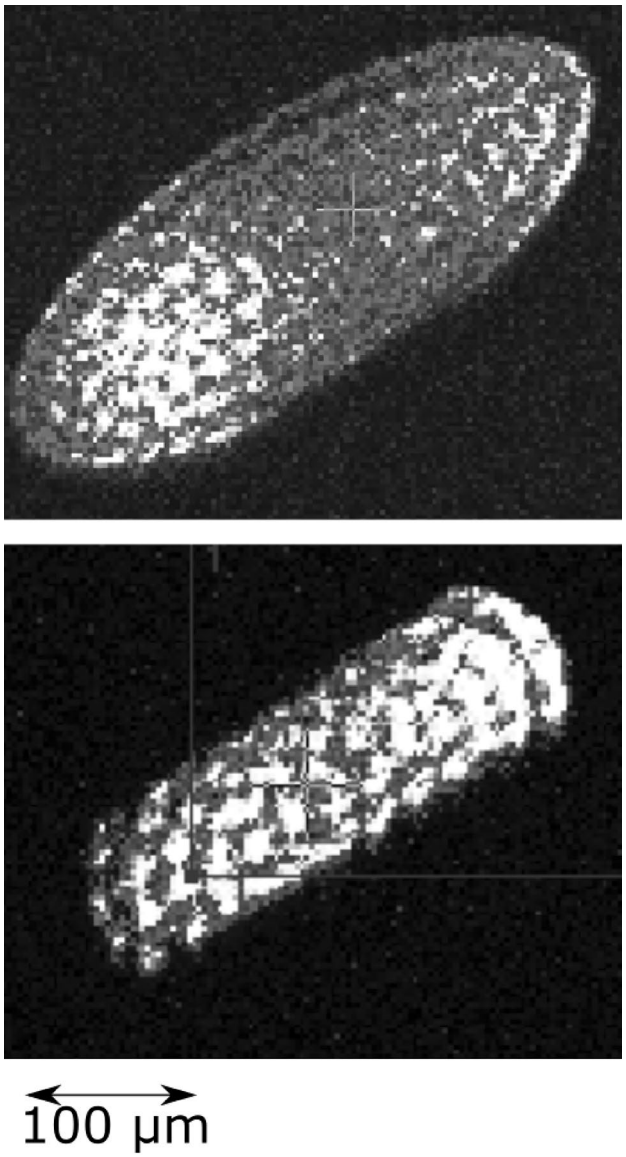


**Fig. 10** CCD images of ion crystals. The top image shows a crystal that contains only $^{171}Yb^{+}$ ions and was taken shortly after loading. The lower image shows the same sample but a few hours later. It can be seen that the remaining $^{171}Yb^{+}$ ions are confined to the center of the original crystal outline. The distorted shape of the fluorescing ions is due to heavier, non-fluorescing ions, occupying the lattice sites that complete the prolate spheroid shape of the minimum-potential volume

which we believe is dominated by temporary magnetization of between 10 and 25 nT generated by the oven current.

The dominant frequency shift for this clock arises from the second-order Zeeman effect and this is determined by our applied bias field $\mathbf{B} \approx 8\,\mu\mathrm{T}$. This high bias field is required, because, in the presence of a magnetic field gradient, the clock transition can be broadened when the Zeeman splitting equals that of a secular frequency. This is discussed in Ref. [54] and creates an additional clear-out path from the $F = 1, \Delta m_F = 0$ clock level, broadening this transition. Operating at a magnetic field giving a Zeeman splitting of more than the secular frequencies restricts us to $\mathbf{B} \geq 8\,\mu\mathrm{T}$ and, therefore, sets a limit on the Zeeman shift (Eq. (5)) and its contribution to the frequency stability arising from changes in the ambient magnetic field. However, by incorporating a second lock to the $F = 1, m_F = \pm 1$ magnetically sensitive Zeeman components, corrections for magnetic field variations could be applied, and this lock is intended for future implementation.

This section has outlined our plans for trap system improvements to improve device robustness, frequency stability and reproducibility. In particular, off-line tests of a new oven design indicate that significant improvements in performance are possible. In addition, we discussed in Ref. [28] plans for the implementation of a more compact wavemeter and a possible alternative scheme to generate the 369.5 nm cooling radiation.

## 6 Conclusions

This paper describes the performance of a compact microwave frequency standard demonstrator based on laser-cooled ytterbium ions in a linear Paul trap. The short-term frequency instability achieved over averaging periods of 30–1500 s was $3.6 \times 10^{-12}/\sqrt{\tau}$ which is an improvement over that of the best commercial compact atomic clocks. A shot-noise limited instability of $1 \times 10^{-12}/\sqrt{\tau}$ is implied from our measurements of the initial lineshape. Enhancements to this system will address the fluorescence loss issue and allow longer term operation. The next design iteration will enable the reproducibility to be investigated at the $10^{-14}$ level and determine the limits to the ultimate accuracy achievable. Together with a substantial reduction in size, and further development of the laser system [28], these improvements should allow demonstration of the full capability of our laser-cooled frequency standard.

**Acknowledgements** The authors would like to gratefully acknowledge U.K. Defence Science and Technology Laboratory (Dstl) and Innovate UK for funding the development here reported. We would also like to thank our colleagues Pravin Patel for his assistance with the electronics, Peter Nisbet-Jones for his work on the vacuum system, and Steven King for his work at the beginning of the project.

## References

1. L.S. Cutler, Fifty years of commercial caesium clocks. Metrologia **42**(3), S90–S99 (2005)
2. J. Camparo, The rubidium atomic clock and basic research. Phys. Today **60**, 33–39 (2007)

3. Microsemi Corporation, SA.45s CSAC datasheet (2019). https://www.microsemi.com/document-portal/doc_download/133305-sa-45s-csac-datasheet
4. Y.Y. Jau, H. Partner, P.D. Schwindt, J.D. Prestage, J.R. Kellogg, N. Yu, Low-power, miniature $^{171}$Yb ion clock using an ultra-small vacuum package. Appl. Phys. Lett. **101**(25), 253518 (2012)
5. P.D. Schwindt, Y.Y. Jau, H. Partner, A. Casias, A.R. Wagner, M. Moorman, R.P. Manginell, J.R. Kellogg, J.D. Prestage, A highly miniaturized vacuum package for a trapped ion atomic clock. Rev. Sci. Instrum. **87**(5), 053112 (2016)
6. R.L. Tjoelker, J.D. Prestage, E.A. Burt, P. Chen, Y.J. Chong, S.K. Chung, W. Diener, T. Ely, D.G. Enzer, H. Mojaradi, C. Okino, M. Pauken, D. Robison, B.L. Swenson, B. Tucker, R. Wang, Mercury ion clock for a NASA technology demonstration mission. IEEE Trans. Ultrason. Ferroelectr. Freq. Control **63**(7), 1034–1043 (2016)
7. J.C. Camparo, C.M. Klimcak, S.J. Herbulock, Frequency equilibration in the vapor-cell atomic clock. IEEE Trans. Instrum. Meas. **54**(5), 1873–1880 (2005)
8. Y.Y. Jau, J.D. Hunker, P.D.D. Schwindt, F-state quenching with $CH_4$ for buffer-gas cooled $^{171}Yb^+$ frequency standard. AIP Adv. **5**(11), 117209 (2015)
9. R. Warrington, P. Fisk, M. Wouters, M. Lawn, Temperature of laser-cooled $^{171}Yb^+$ ions and application to a microwave frequency standard. IEEE Trans. Ultrason. Ferroelectr. Freq. Control **49**(8), 1166–1174 (2002)
10. S. J. Park, P. J. Manson, M. J. Wouters, R. B. Warrington, M. A. Lawn, P. T. H. Fisk, "$^{171}Yb^+$ Microwave Frequency Standard," in *2007 IEEE International Frequency Control Symposium Joint with the 21st European Frequency and Time Forum*, pp. 613–616 (2007)
11. T.P. Heavner, E.A. Donley, F. Levi, G. Costanzo, T.E. Parker, J.H. Shirley, N. Ashby, S. Barlow, S.R. Jefferts, First accuracy evaluation of NIST-F2. Metrologia **51**(3), 174 (2014)
12. J. Guena, M. Abgrall, D. Rovera, P. Laurent, B. Chupin, M. Lours, G. Santarelli, P. Rosenbusch, M.E. Tobar, R. Li, K. Gibble, A. Clairon, S. Bize, Progress in atomic fountains at LNE-SYRTE. IEEE Trans. Ultrason. Ferroelectr. Freq. Control **59**(3), 391–410 (2012)
13. K. Szymaniec, S.E. Park, G. Marra, W. Chałupczak, First accuracy evaluation of the NPL-CsF2 primary frequency standard. Metrologia **47**(4), 363–376 (2010)
14. R. Warrington, P. Fisk, M. Wouters, M. Lawn, C. Coles, "The CSIRO trapped $^{171}Yb^+$ ion clock: improved accuracy through laser-cooled operation," in *Proceedings of the 1999 Joint Meeting of the European Frequency and Time Forum, 1999 and the IEEE International Frequency Control Symposium, 1999*, pp. 125–128, (1999)
15. P. Phoonthong, M. Mizuno, K. Kido, N. Shiga, Determination of the absolute microwave frequency of laser-cooled $^{171}Yb^+$. Appl. Phys. B **117**(2), 673–680 (2014)
16. S. Mulholland, *Development of a portable laser-cooled ytterbium ion microwave atomic clock*. PhD thesis, University of Oxford (2018)
17. S. Olmschenk, D. Hayes, D.N. Matsukevich, P. Maunz, D.L. Moehring, K.C. Younge, C. Monroe, Measurement of the lifetime of the $6p^2P^o_{1/2}$ level of $Yb^+$. Phys. Rev. A **80**, 022502 (2009)
18. N. Yu, L. Maleki, Lifetime measurements of the $4f^{14}5d$ metastable states in single ytterbium ions. Phys. Rev. A **61**(2), 022507 (2000)
19. M. Roberts, P. Taylor, G.P. Barwood, P. Gill, H.A. Klein, W.R.C. Rowley, Observation of an electric octupole transition in a single ion. Phys. Rev. Lett. **78**(10), 1876–1879 (1997)
20. N. Huntemann, C. Sanner, B. Lipphardt, C. Tamm, E. Peik, Single-ion atomic clock with $3 \times 10^{-18}$ systematic uncertainty. Phys. Rev. Lett. **116**, 063001 (2016)
21. R.M. Godun, P.B.R. Nisbet-Jones, J.M. Jones, S.A. King, L.A.M. Johnson, H.S. Margolis, K. Szymaniec, S.N. Lea, K. Bongs, P. Gill, Frequency ratio of two optical clock transitions in $^{171}Yb^+$ and constraints on the time variation of fundamental constants. Phys. Rev. Lett. **113**(210801), 1–5 (2014)
22. P. Fisk, M. Sellars, M. Lawn, C. Coles, Performance of a prototype microwave frequency standard based on laser-detected, trapped 171 Yb+ ions. Appl. Phys B Lasers Opt. **60**(6), 519–527 (1995)
23. D.J. Berkeland, M.G. Boshier, Destabilization of dark states and optical spectroscopy in Zeeman-degenerate atomic systems. Phys. Rev. A **65**, 033413 (2002)
24. J. Keller, H.L. Partner, T. Burgermeister, T.E. Mehlstäubler, Precise determination of micromotion for trapped-ion optical clocks. J. Appl. Phys. **118**(10), 1–13 (2015)
25. D.R. Denison, Operating parameters of a quadrupole in a grounded cylindrical housing. J. Vacuum Sci. Technol. **8**(1), 266–269 (1971)
26. J. Pedregosa, C. Champenois, M. Houssin, M. Knoop, Anharmonic contributions in real RF linear quadrupole traps. Int. J. Mass Spectrom. **290**(2–3), 100–105 (2010)
27. G. Werth, V. N. Gheorghe, F. G. Major, *Charged Particle Traps II: Applications*, Springer Series on Atomic, Optical, and Plasma Physics, vol 54 (Springer, 2009)
28. S. Mulholland, H.A. Klein, G.P. Barwood, S. Donnellan, P.B.R. Nisbet-Jones, G. Huang, G. Walsh, P.E.G. Baird, P. Gill, Compact laser system for a laser-cooled ytterbium ion microwave frequency standard. Rev. Sci. Instrum. **90**(3), 033105 (2019)
29. S. Rauch, J. Sacher, Compact bragg grating stabilized ridge waveguide laser module with a power of 380 mW at 780 nm. IEEE Photon. Technol. Lett. **27**, 1737–1740 (2015)
30. K.G. Libbrecht, J.L. Hall, A low-noise high-speed diode laser current controller. Rev. Sci. Instrum. **64**(8), 2133–2135 (1993)
31. C.J. Erickson, M. Van Zijll, G. Doermann, D.S. Durfee, An ultrahigh stability, low-noise laser current driver with digital control. Rev. Sci. Instrum. **79**(7), 073107 (2008)
32. Y.-Y. Jau, F.M. Benito, H. Partner, P.D.D. Schwindt, Low power high-performance radio frequency oscillator for driving ion traps. Rev. Sci. Instrum. **82**, 023118 (2011)
33. G.P. Barwood, P. Gill, G. Huang, H.A. Klein, Automatic laser control for a $^{88}Sr^+$ optical frequency standard. Meas. Sci. Technol. **23**(5), 055201 (2012)
34. K. Toyoda, A. Miura, S. Urabe, K. Hayasaka, M. Watanabe, Laser cooling of calcium ions by use of ultraviolet laser diodes: significant induction of electron-shelving transitions. Opt. Lett. **26**(23), 1897 (2001)
35. F. Riehle, *Frequency Standards: Basics and Applications* (Wiley, New York, 2005)
36. C. F. A. Baynham, *Frequency metrology at the* $10^{-18}$ *level with an ytterbium ion optical clock*. PhD thesis, University of Oxford (2018)
37. M. Tomza, K. Jachymski, R. Gerritsma, A. Negretti, T. Calarco, Z. Idziaszek, P. S. Julienne, "Cold hybrid ion-atom systems," arXiv:1708.07832 (2017)
38. S. A. King, *Sub-hertz optical frequency metrology using a single ion of 171 Yb +*. PhD thesis, University of Oxford (2012)
39. K. Sugiyama, J. Yoda, Disappearance of $Yb^+$ in excited states from RF trap by background gases. Japan. J. Appl. Phys. **34**(5A), L584–L586 (1995)
40. J. Vanier, C. Audoin, *The Quantum Physics of Atomic Frequency Standards* (Hilger, Bristol, 1989)
41. H.C.J. Gan, G. Maslennikov, K.-W. Tseng, T.R. Tan, R. Kaewuam, K.J. Arnold, D. Matsukevich, M.D. Barrett, Oscillating-magnetic-field effects in high-precision metrology. Phys. Rev. A **98**, 032514 (2018)

42. D.J. Berkeland, J.D. Miller, J.C. Bergquist, W.M. Itano, D.J. Wineland, Laser-cooled mercury ion frequency standard. Phys. Rev. Lett. **80**(1523), 2089–2092 (1998)
43. R.G. DeVoe, J. Hoffnagle, R.G. Brewer, Role of laser damping in trapped ion crystals. Phys. Rev. A **39**, 4362–4365 (1989)
44. D.J. Berkeland, J.D. Miller, J.C. Bergquist, W.M. Itano, D.J. Wineland, Minimization of ion micromotion in a Paul trap. J. Appl. Phys. **83**(10), 5025–5033 (1998)
45. P.T.H. Fisk, M.J. Sellars, M.A. Lawn, G. Coles, Accurate measurement of the 12.6 GHz "clock" transition in trapped $^{171}$Yb ions. IEEE Trans. Ultrason. Ferroelectr. Freq. Control **44**, 344–354 (1997)
46. C. Tamm, D. Schnier, A. Bauch, Radio-frequency laser double-resonance spectroscopy of trapped $^{171}$Yb ions and determination of line shifts of the ground-state hyperfine resonance. Appl. Phys. B **60**(1), 19–29 (1995)
47. E.J. Angstmann, V.A. Dzuba, V.V. Flambaum, Frequency shift of hyperfine transitions due to blackbody radiation. Phys. Rev. A **74**(023405), 1–8 (2006)
48. U.I. Safronova, M.S. Safronova, Third-order relativistic many-body calculations of energies, transition rates, hyperfine constants, and blackbody radiation shift in $^{171}Yb^{+}$. Phys. Rev. A **79**, 022512 (2009)
49. G. J. Dick, "Local oscillator induced instabilities in trapped ion frequency standards," in *Proceedings of the 19th Annual Precise Time and Time Interval Systems and Applications Meeting, Redondo Beach*, pp. 133–147 (1987)
50. K. Sugiyama, J. Yoda, Production of $YbH^{+}$ by chemical reaction of$Yb^{+}$ in excited states with $H_2$ gas. Phys. Rev. A **55**, R10–R13 (1997)
51. B. Dubost, R. Dubessy, B. Szymanski, S. Guibal, J.-P. Likforman, L. Guidoni, Isotope shifts of natural $Sr^{+}$ measured by laser fluorescence in a sympathetically cooled coulomb crystal. Phys. Rev. A **89**, 032504 (2014)
52. L. Hornekær, N. Kjærgaard, A.M. Thommesen, M. Drewsen, Structural properties of two-component Coulomb crystals in linear Paul traps. Phys. Rev. Lett. **86**(10), 1994–1997 (2001)
53. K. Sheridan, M. Keller, Weighing of trapped ion crystals and its applications. New J. Phys. **13**, 123002 (2011)
54. H. L. Partner, *Development and Characterization of a* $^{171}Yb^{+}$ *Miniature Ion Trap Frequency Standard*. PhD thesis, University of New Mexico, Albuquerque (2013)